



A generalized photon-tracking approach to simulate spectral snow albedo and transmissivity using X-ray microtomography and geometric optics

Theodore Letcher¹, Julie Parno¹, Zoe Courville¹, Lauren Farnsworth¹, and Jason Olivier¹

¹US Army Corps of Engineers Cold Regions Research and Engineering Laboratory, Hanover, NH

Correspondence: Theodore Letcher (Theodore.W.Letcher@erdc.dren.mil)

Abstract. A majority of snow radiative transfer models (RTM) treat snow as a collection of idealized grains rather than an organized ice-air matrix. Here we present a generalized multi-layer photon-tracking RTM that simulates light transmissivity and reflectivity through snow based on X-ray microtomography, treating snow as a coherent structure rather than a collection of grains. Notably, the model uses a blended approach to expand ray-tracing techniques applied to sub-1 cm³ snow samples to snowpacks of arbitrary depths. While this framework has many potential applications, this study's effort is focused on simulating light transmissivity through thin snowpacks as this is relevant for surface energy balance applications and sub-nivean hazard detection. We demonstrate that this framework capably reproduces many known optical properties of a snow surface, including the dependence of spectral reflectance on snow grain size and incident zenith angle and the surface bidirectional reflectance distribution function (BRDF). To evaluate how the model simulates transmissivity, we compare it against spectroradiometer measurements collected at a field site in east-central Vermont. In this experiment, painted panels were inserted at various depths beneath the snow to emulate thin snow. The model compares remarkably well against the spectroradiometer measurements. Sensitivity simulations using this model indicate that snow transmissivity is greatest in the visible wavelengths and is limited to the top 5 cm of the snowpack for fine-grained snow, but can penetrate as deep as 8 cm for coarser grain snow. An evaluation of snow optical properties generated from a variety of snow samples suggests that coarse grained low density snow is most transmissive.

1 Introduction

Due to the highly reflective nature of snow, seasonal snowpacks make the surface significantly more reflective when present, impacting regional weather and climate. Correspondingly, the snow albedo feedback, caused by changes in seasonal snow cover extent and properties, represents one of the more dramatic markers of regional and global climate change (e.g., Hall, 2004; Déry and Brown, 2007; Flanner et al., 2011; Letcher and Minder, 2015; Thackeray and Fletcher, 2016). While snow is highly reflective, snow albedo is not equal for all snowpacks. For instance, snow albedo typically decreases with snow age due



to metamorphic processes resulting in larger snow grains (e.g., Wiscombe and Warren, 1980; Aoki et al., 2000; Flanner and Zender, 2006; Adolph et al., 2017). Snow albedo is also diminished by light absorbing impurities such as dust or black carbon
25 that contaminate the snow (e.g., Doherty et al., 2010; Painter et al., 2012; Skiles et al., 2012; Dumont et al., 2014; Skiles et al., 2015; Skiles and Painter, 2019; Shi et al., 2021). Importantly, these two effects impact different parts of the electromagnetic spectrum, with grain size having a greater influence in the near-infrared (NIR), and the particle contamination influencing the visible region. Finally, even though thin snow covers are highly reflective, the aggregate surface albedo for a thin snow
30 cover can be influenced by the underlying ground surface depending on the snow microstructure (Perovich, 2007; Warren, 2013; Libois et al., 2013). Understanding these small-scale drivers of snow albedo is important for large-scale remote sensing applications and regional weather and climate modeling.

There are several documented approaches to model snow broadband and spectral albedo using radiative transfer models (RTMs) in efforts to better understand and predict the effects of snow aging and impurities on snow optical properties. While a full review of snow radiative transfer is well beyond the scope of this paper, we refer the reader to He and Flanner (2020)
35 for a rigorous overview of the different approaches. There are also numerous simplified parameterizations for snow albedo of varying complexity designed for implementation in weather and climate models (e.g., Verseghy, 1991; Dickinson, 1993; Gardner and Sharp, 2010; Vionnet et al., 2012; Saito et al., 2019; Bair et al., 2019).

At a fundamental level, the scattering of electromagnetic energy incident upon the boundary separating a snow grain and the surrounding air is determined by the different refractive indices for ice and air. The absorption of light as it passes through solid
40 ice is well understood and has a strong wavelength dependence (e.g., Grenfell and Perovich, 1981; Perovich and Govoni, 1991; Warren and Brandt, 2008). The scattering of visible and NIR light at an air/ice boundary is well described by the geometric optics approximation, which requires that the wavelength of light is small relative to the size of the scattering particle. While the physics behind scattering and absorption are well understood for a single snow particle, the actual path of a light ray through a snowpack can be extraordinarily convoluted as the ray is constantly intersecting air/ice interfaces with very little absorption.

Seminal studies describing snow albedo modeling (e.g., Warren and Wiscombe, 1980; Wiscombe and Warren, 1980) and most subsequent approaches treat snow grains as independent scatterers, where the scattering properties of an individual grain are not affected by adjacent grains and are independent of the spacing between grains and, thus, snow density. Mie theory is typically used to calculate snow albedo owing to its computational efficiency (e.g., Bohren and Beschta, 1979; Wiscombe, 1980). However, Mie theory is most often applied to particles with spherical geometries, and so it is common practice to
50 represent snow by a collection of effective spheres. Yet although snow grain size is often most cited as the key driver of pure snow albedo, grain shape also has an impact on snow spectral albedo (Aoki et al., 2000; Libois et al., 2013; Dang et al., 2016). For instance, an inter-comparison of several commonly-used two stream RTMs parameterizing snow grains as equivalent spheres conclude that these models overestimate snow albedo in the NIR (Dang et al., 2019).

Efforts to understand and simulate the impacts of snow particle shape on snow spectral albedo have largely focused on
55 leveraging the geometric optics approximation in various ways. For instance, Yang and Liou (1996) used ray-tracing to compute the single scattering properties of idealized hexagonal columns, plates, and rosettes. Grundy et al. (2000) presented a Monte Carlo approach to estimate optical properties of computer-rendered 3D spheres that compared well with Mie theory. Their



work was extended to estimate the scattering properties of irregularly shaped crystals. A more recent effort by Xiong et al. (2015) focused on determining the optical properties of an idealized mixed snow/air medium generated from a randomized bicontinuous 2D representation of the snow. More recently, several studies have used ray-tracing and photon-tracking methods to simulate snow optical properties from renderings of snow particles generated from X-ray microtomography (hereby: μ CT) scans of real snow (Haussener et al., 2012; Kaempfer et al., 2007; Ishimoto et al., 2018; Dumont et al., 2021).

Collectively, RTM-focused studies of snow have greatly expanded the knowledge surrounding the optical properties of irregular snow grains and informed the role of snow microstructure on spectral reflectance. However, the impact of snow microstructure on snow spectral transmissivity has often been overlooked in observations and modeling.

In this study, we build upon the approaches of Grundy et al. (2000), Kaempfer et al. (2007), Jacques (2010), and Xiong et al. (2015) to develop a Monte Carlo photon-tracking snow RTM that is driven by μ CT observations of snow and is designed for broad applications, including snow transmissivity. The primary purpose of this RTM framework is to use explicit photon-tracking techniques in conjunction with 3D renderings of snow samples to estimate realistic snow optical properties for use in a Monte Carlo photon-tracking model. In section 2 we describe the model framework and μ CT data processing. In section 3, we demonstrate the model's capability to reproduce known optical properties of snow, compare model output to spectral albedo measurements of objects buried beneath snow at various depths, and use the RTM to investigate snow transmissivity. In sections 4 and 5, we present a broad discussion and conclusions.

2 Data and Methods

Here we describe the framework of a new, semi-quantized Monte Carlo photon-tracking model designed to simulate radiative transfer (RT) through snow with a focus on spectral albedo and transmissivity in the visible and NIR (i.e., $380 \leq \lambda \leq 1300$ nm). While computationally expensive, there are several advantages to the Monte Carlo approach over more traditional approaches that aim to solve the radiative transfer equation (RTE). In particular Monte Carlo models are useful for modeling RT through non-spherical particles and for 3D RT applications (e.g., Iwabuchi, 2006; Whitney, 2011). In this model, the Monte Carlo approach is used in order to eliminate all assumptions regarding snow microstructure. Specifically, this approach treats the snowpack more as a coherent structural ice lattice rather than as a collection of idealized particles. The explicit photon-tracking through 3D renderings of snow performed as part of this model are similar to those described in Grundy et al. (2000); Kaempfer et al. (2007); Dumont et al. (2021); Ishimoto et al. (2018). Additionally, the Monte Carlo approach lends itself well to parallelization, and the semi-quantized approach described here reduces the number of photons required to achieve a statistically robust result. Yet, this approach is not without its drawbacks. For instance, the geometric optics approximation localizes the ray, directing all scattered radiation along a single path. Further, this framework ignores the wave properties of light, such as phase and diffraction, which limits its overall applicability and reduces accuracy. Despite these drawbacks, numerous approaches in the literature have demonstrated success in simulating snow reflectance of natural (i.e., unpolarized) light using these simplifications (e.g., Kaempfer et al., 2007; Malinka, 2014; Xiong et al., 2015).



90 This model can be divided into two distinct components. The first of which determines key snow medium optical properties
by launching photons into 3D closed-surface renderings of snow samples derived from μ CT scans with a voxel resolution of
 $\approx 20 \mu\text{m}$. The second uses the optical properties derived from the first part to drive a 1D photon-tracking model whereby
individual photon packets are prescribed a random initial position and incident direction on the snow. Each individual photon
packet then has a unique path whereby all of the energy contained within a given packet travels in the same direction and the
95 amount of energy within a given packet is depleted continuously according to absorption within the medium. Note that for
both model components, the ice refractive indices reported by Warren and Brandt (2008) are used to compute scattering and
absorption.

2.1 Snow Optical Properties

The 1D medium model requires three key optical properties: the extinction coefficient (γ_{ext}), the mean path fraction traveled
100 within ice (F_{ice}), and the scattering phase function ($p(\cos\Theta)$). In considering light as a ray traveling through the snow medium,
which is scattered each time it intersects an air/ice boundary and partially absorbed within the ice, the extinction coefficient is
related to the distance traveled between scattering and absorption events. The phase function determines the change in direction
of the ray during a scattering event, and the ice-path fraction, when combined with the ice absorption coefficient, determines
the mean energy depleted from the ray for a given distance traveled between scattering events. For a given snow sample,
105 γ_{ext} is determined following the method described in Xiong et al. (2015) applied to the 3D rendering of snow as opposed to
an idealized bicontinuous medium. In this framework, photons are initialized at a random position within the snow sample,
and launched in a random direction for a specified distance (L). If the photon is initialized within the air, the probability of
extinction (P_{ext}) is 1 if a boundary is intersected over L , otherwise it is 0. In the case where the photon is initialized within the
ice medium, $P_{ext}=1$ if a boundary is intersected over L , otherwise it is given as:

$$110 \quad P_{ext} = 1 - e^{-\kappa_{\lambda}L}, \quad (1)$$

where κ_{λ} is the wavelength-dependent absorption coefficient of ice, which is related to the imaginary part of the ice refractive
index (k):

$$\kappa_{\lambda} = \frac{4\pi k}{\lambda}. \quad (2)$$

This slight modification is made to account for the added probability of extinction due to absorption of the photon within the
115 ice particle. Note that this also introduces a minor wavelength dependence into the extinction coefficient. Using this method,
a probability of extinction can be determined for distance L . This method is repeated for several distances ranging from the
voxel resolution ($20 \mu\text{m}$) to the width of the snow sample volume (e.g., 10 mm). The extinction coefficient is then determined
using a curve fit to Beer-Lambert law:



$$P_{ext} = 1 - e^{-\gamma_{ext}L}, \quad (3)$$

120 The mean fractional ice path (F_{ice}) is determined by tracking individual photons as they travel throughout the aggregate snow sample. This framework closely mimics that of Kaempfer et al. (2007) in that photons travel through the snow medium and change direction according to Snell's law of refraction and a probabilistic representation of Fresnel's law of reflectance. Here, a photon is initialized at a random starting point somewhere within the snow sample and launched in a random direction. The photon is tracked until it exits the medium, and the F_{ice} is simply the ratio of the distance traveled within ice over the total
 125 distance traveled. This is repeated for a large number of photons to determine an average F_{ice} .

Fresnel's law dictates that the fractional reflection and transmission of light at a boundary is related to the incident angle (θ_i) and the refractive indices (n) of the two media separated by the boundary:

$$R_h = \frac{n_1 \cos \theta_i - n_2 \sqrt{1 - \left(\frac{n_1}{n_2} \sin \theta_i\right)^2}}{n_1 \cos \theta_i + n_2 \sqrt{1 - \left(\frac{n_1}{n_2} \sin \theta_i\right)^2}}, \quad (4)$$

and

$$130 \quad R_v = \frac{n_1 \sqrt{1 - \left(\frac{n_1}{n_2} \sin \theta_i\right)^2} - n_2 \cos \theta_i}{n_1 \sqrt{1 - \left(\frac{n_1}{n_2} \sin \theta_i\right)^2} + n_2 \cos \theta_i}, \quad (5)$$

where R_h and R_v are the horizontally and vertically polarized reflectances. Assuming that the radiation is unpolarized (e.g., natural light), the reflectance (R) is:

$$R = \frac{1}{2}(R_h^2 + R_v^2). \quad (6)$$

Through energy conservation, the transmittance (T) is simply:

$$135 \quad T = 1 - R. \quad (7)$$

Then, if the vector normal to the boundary plane (\hat{v}_n) is oriented towards the medium with refractive index n_1 , the direction unit vectors for transmitted and reflected radiation are computed as:

$$\hat{v}_r = \hat{v}_i + 2 \cos \theta_i \hat{v}_n \quad (8)$$



and

$$140 \quad \hat{v}_t = \frac{n_1}{n_2} \hat{v}_i + \left(\frac{n_1}{n_2} \cos\theta_i - \cos\theta_t \right) \hat{v}_n, \quad (9)$$

where \hat{v}_r and \hat{v}_t are the reflection and transmission unit direction vectors, respectively.

The phase function is determined by separating out individual snow grains from the reconstructed 3D snow sample and probing them with photons to compute the scattering angle where the cosine of the scattering angle (Θ) is the dot product between the directional unit vector of radiation incident on the particle ($\hat{\Omega}'$) and the directional unit vector of the scattered radiation ($\hat{\Omega}$) in the cartesian coordinate space:

$$145 \quad \cos\Theta = \hat{\Omega}' \cdot \hat{\Omega}. \quad (10)$$

The phase function is constructed by first initializing a photon outside of a given particle and firing it in a random direction towards the particle. The photon then interacts with the snow particle, guided by Eqs. 4 - 9. For each collision (i), the amount of energy exiting the particle into the directional bin ($\cos\Theta_j$) is tracked, and the remaining photon energy is depleted as energy exits, or is absorbed within, the ice particle. This is repeated for an arbitrary number of collisions (n) until there is less than 0.1% of the initial energy left (Fig. 1). For the initial collision ($i = 0$), the energy exiting the particle is simply the reflected fraction of the incident ray, and for each subsequent collision, it is the transmitted multiplied by the remaining ray energy (e.g., Malinka, 2014):

$$150 \quad W_{\Theta_i} = \begin{cases} R_0 & i = 0 \\ T_0 T_i & i = 1, \\ T_0 \left(\prod_{n=1}^{i-1} R_n e^{-\kappa_\lambda s_n} \right) T_i & i > 1 \end{cases}, \quad (11)$$

where s_n is the distance traveled within the particle between the boundary intersections $n - 1$ and n . For visible wavelengths, the impact of absorption on the phase function is negligible, however for wavelengths exceeding 1000 nm, it becomes more important. The resulting distribution of energy is converted to a phase function defined relative to the ray initially incident upon the scattering particle following Grundy et al. (2000):

$$155 \quad p(\cos\Theta_j) = \frac{4\pi N_j}{N \sin\Theta_j d\Theta}, \quad (12)$$

where N is the total photon energy and N_j is the total photon energy directed into bin j .

In practice, while a majority of photons require only a few collisions to reach the 0.1 % energy threshold, we cap the number of internal collisions to a maximum of 10 to limit both computation time and the accumulation of error caused by imperfect

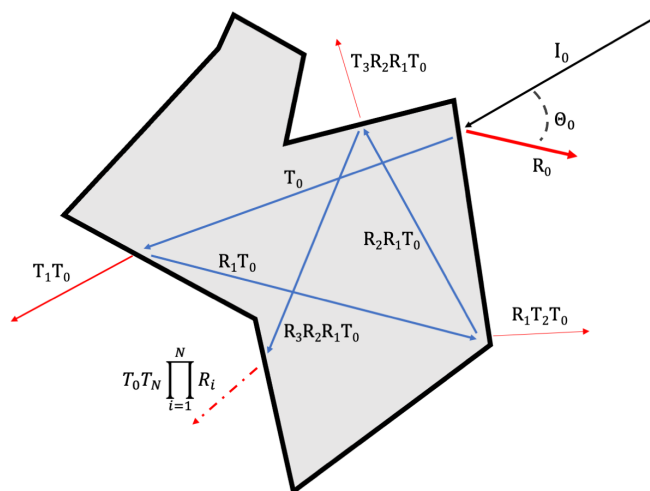


Figure 1. Schematic illustration of the photon-tracking method used to determine the scattering phase function for a grain with an arbitrary shape.

3D particle representations. To evaluate this method, we use it to estimate the phase function of a collection of idealized crystal habits, including spheres, hexagonal plates, and columns with a size parameter of 1000 (Fig. 2). We find that these phase functions are in good agreement with Mie theory for spheres, and with phase functions reported for other shapes presented in previous studies focused on the scattering properties of spherical, idealized, and irregular snow crystal shapes (Jaquinta et al., 1995; Macke et al., 1996; Yang and Liou, 1996; Grundy et al., 2000; Malinka, 2014; Ishimoto et al., 2018). To determine the phase function for 1D model, this ray-tracing method is applied to a selection of rendered grains from the μ CT sample, and $p(\cos\Theta_j)$ is computed for each bin following eq. 12 where N_j is determined from all selected grains. Note that in this method the selected grains are checked to ensure that they contain no facets touching the sample boundaries.

2.2 1D photon-tracking Model

Once the required optical properties of the snow sample are determined by launching photons through μ CT sample volumes, a 1D photon-tracking model is used to simulate snow spectral albedo, transmissivity, and Bidirectional Reflectance Distribution Function (BRDF). The 1D model is used in place of the explicit photon-tracking model described by Kaempfer et al. (2007) in order to allow for the computationally feasible simulation of spectral albedo and transmissivity for snow covers with depths exceeding 1 cm with sufficient grain resolution. Additionally, it is used to address complications associated with lateral boundary treatment and stitching multiple μ CT scans together into a coherent snow lattice. Our 1D model is based largely on Jacques (2010), which describes a semi-random 1D multi-layer Monte Carlo photon-tracking approach for application in the field of biomedical imaging. In this framework, discrete, plane-parallel, snow layers with optical properties constant throughout each layer are first prescribed. Then a photon packet is initialized at some starting position (\mathbf{X}_0) with cartesian components of $(x_0,$

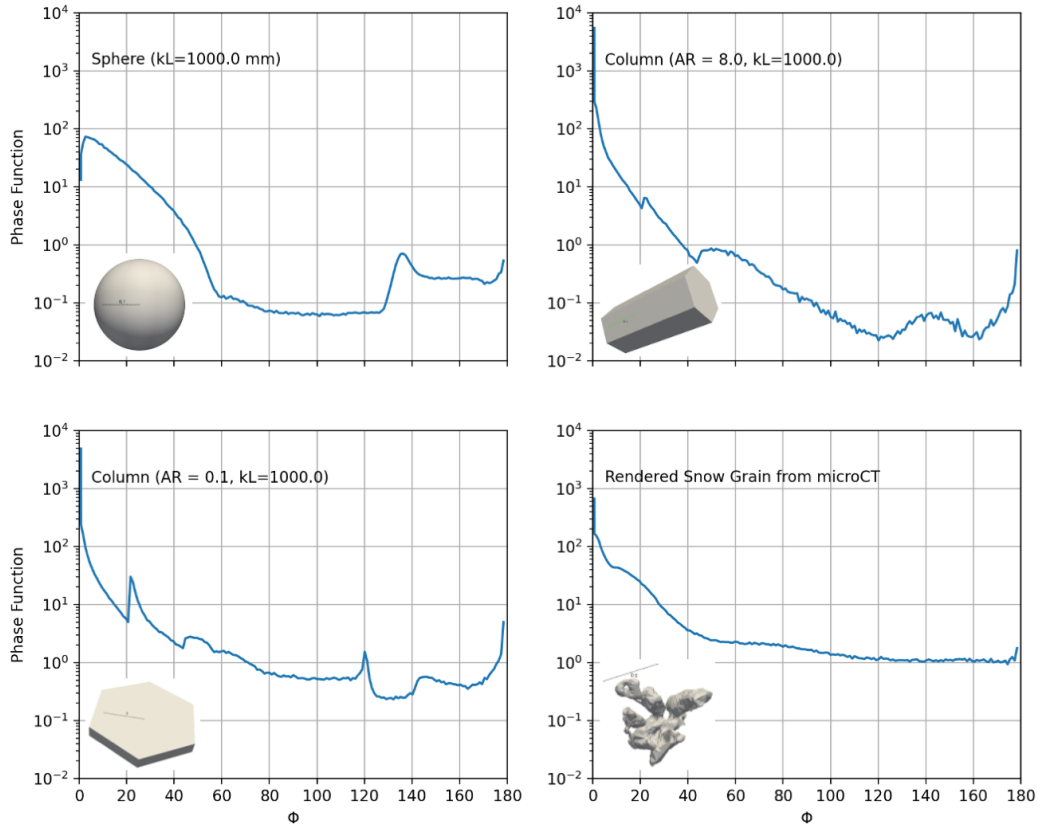


Figure 2. Phase functions for idealized snow particles following equations 11 and 12 for incident radiation at $\lambda=900\text{nm}$. The size parameter (kL) for each particle is set to 1000. Note that for the rendered grain, the approximate grain diameter yielded a size parameter of approximately 1400. 500,000 photons were used to generate the phase function. AR is the axis ratio between the long "c" and short "a" axes of the hexagonal column.

y_0, z_0) and an initial energy of unity ($E = 1$). An initial unit direction vector for the photon is given in cartesian coordinates as:

$$\mathbf{V}_0 = [\sin\theta\cos(\phi), \sin(\theta)\sin(\phi), -\cos\theta], \quad (13)$$

where θ is the solar zenith angle, and ϕ is the azimuth angle clockwise from x . This initial direction can be prescribed randomly (i.e., diffuse radiation), or at any specified zenith/azimuth angle (i.e., direct radiation), or as a mixture of both diffuse and direct radiation.

Once the initial position is set, the photon is launched into the medium, and travels a distance s before experiencing a scattering event. s is computed statistically using the Beer-Lambert law and the medium extinction coefficient (Jacques, 2010):



$$s = -\frac{\ln \zeta}{\gamma_{ext}}, \quad (14)$$

190 where ζ is a random uniform number between 0 and 1. The new position in the medium is:

$$\mathbf{X} = \mathbf{X}_0 + s\mathbf{V}_0 \quad (15)$$

At the scattering event, the photon packet is given a new direction unit vector according to the scattering phase function. Because this framework treats the scattering phase function as a probability distribution function (PDF), the scattering angle Θ is determined by choosing a random sample from $p(\cos\Theta)$ PDF:

$$195 \quad P(\cos\Theta) = \frac{p(\cos\Theta)d\Omega}{4\pi}, \quad (16)$$

where P is the probability of light being scattered into a cone with solid angle $d\Omega$ in the direction Θ from the incident radiation given the phase function.

Then the new direction vector is determined from Θ (Jacques, 2010):

$$\begin{aligned} \mu_x &= \frac{\sin\Theta(\mu_{x0}\mu_{z0}\cos\phi - \mu_{y0}\sin\phi)}{\sqrt{1-\mu_{z0}^2}} \\ \mu_y &= \frac{\sin\Theta(\mu_{y0}\mu_{z0}\cos\phi - \mu_{x0}\sin\phi)}{\sqrt{1-\mu_{z0}^2}}, \\ \mu_z &= -\sqrt{1-\mu_{z0}^2}\sin\Theta\cos\phi + \mu_{z0}\cos\Theta \end{aligned} \quad (17)$$

200 where ϕ is given as a uniform random number between 0 and 2π , the 0 subscript represents the incident direction, and μ_x , μ_y , and μ_z make up the components of the unit direction vector.

Photon energy is depleted over distance s according to the ice absorption coefficient and F_{ice}^i as determined from the μ CT data instead of using a medium absorption coefficient:

$$E = E_0 \left(e^{-\kappa_\lambda s F_{ice}^i} \right), \quad (18)$$

205 where E is the new photon energy, and E_0 is the incident photon energy.

To achieve statistical energy conservation, a "Russian Roulette" function is used to determine whether or not to fully absorb (i.e., kill) the photon packet once its energy falls below a prescribed threshold (Iwabuchi, 2006; Jacques, 2010). This is given as:

$$E = \begin{cases} mE & \zeta \leq 1/m \\ 0 & \zeta > 1/m \end{cases}, \quad (19)$$



210 where ζ is a random number between 0 and 1, and m is a prescribed constant on the order of 1-10. By treating absorption continuously rather than probabilistically, the number of photons required to attain a robust solution is significantly reduced, and further ensures that the model cannot get stuck in an infinite loop.

If the z position of a photon-packet is above the top of the snow surface (i.e., it has exited the top of the snowpack), the remaining energy within the packet is added to the total reflected energy and the photon is eliminated. In an open lower-
215 boundary configuration, if a photon-packet z position is less than 0 (i.e., it has exited the bottom of the snowpack) the remaining energy is added to the total transmitted energy, and the photon is eliminated. Alternatively, a lower boundary can be simulated with a specified spectral reflectance such that a portion of the photon energy will be absorbed at the lower boundary, and the remaining energy will be reflected upward. Once all photons have been eliminated from the model, the simulation is complete.

This model is extended to a multilayer configuration, by simply defining unique optical properties corresponding to specified
220 depths throughout the snowpack. When a photon packet travels from one layer to another, its trajectory and energy depletion are determined by the optical properties of the new layer.

The basic premise of this model is illustrated in figure 3, which traces the position and energy of two photons on a 2D plane as they travel throughout an idealized two-layer snowpack 10 cm deep.

2.3 Directional Conic Reflectance Function

225 The reflectance of a surface is often described using the concept of a BRDF (e.g., Stamnes and Stamnes, 2016). This concept essentially represents a PDF of reflected direction of a ray of light impacting the surface from a given incident direction, and is used to simplify the complex reflectance properties of a rough surface (e.g., shading and multiple reflections). To estimate the BRDF from this model, we follow the methods described in Kaempfer et al. (2007). In this framework, the BRDF for specified incident zenith and azimuth directions is approximated using the Directional Conic Reflectance Function (DCRF),
230 which computes the energy reflected into a cone in the direction: θ_r, ϕ_r subtended by solid angle: $d\Omega$:

$$DCRF(\theta_i, \phi_i, \theta_r, \phi_r) = \frac{I_r(\theta_r, \phi_r)}{I_i(\theta_i, \phi_i) \cos \theta_i d\Omega}, \quad (20)$$

where I is the radiative flux, and the subscripts i , and r correspond to the incident and reflected radiation, respectively.

2.4 Snow sampling and spectroradiometer measurements in the field

To evaluate the model, we collected snow samples and snow surface spectroradiometer measurements at Union Village Dam
235 (UVD) in Thetford, Vermont several times throughout the 2020-21 winter. The UVD site is a broad flat clearing surrounded by deciduous forests spanning approximately 40000 m², and bounded on the southern end by the Ompompanoosuc River. During each data collection, a snow pit was excavated and standard snow characteristics, such as snow depth, density, and grain size were measured manually. Several snow samples were carefully extracted in columns adjacent to the snow pit sidewalls in cylindrical containers 7 cm high x 1.9 cm in diameter (Fig. 4). These samples were transported in a hard, plastic cooler for 10

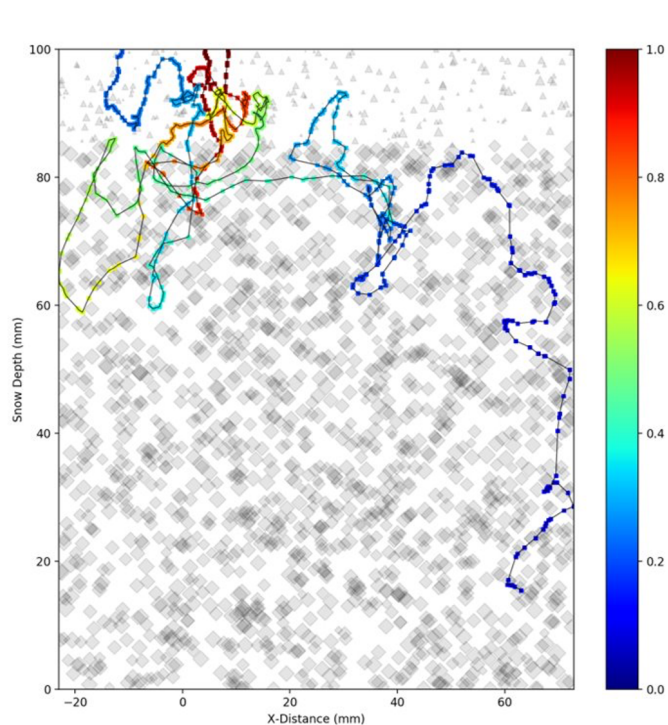


Figure 3. x/z cross section of two photons within a multi-layered snowpack 10 cm deep. The color scale indicates the fractional energy of the photon packet. The gray markers aid in showing the different snow layers. Note that only one photon exits the top of the snowpack, the other is fully absorbed in the lower layer. Note that the markers are provided as a visual aid, and not representative of the snow particle shape or distribution.

240 miles from the UVD site to the Cold Regions Research and Engineering Laboratory (CRREL). At CRREL they were stored in a -20°C cold room prior to μCT analysis. These samples were not casted (i.e. not preserved using a pore-filler).

Spectral reflectance and transmissivity data were collected using a Malvern Panalytical ASD FieldSpec 4 Hi-Res: High Resolution Spectroradiometer. The FieldSpec 4 has a spectral range of 350-2500 nm and a spectral resolution of 3 nm in the visible and 10 nm in the SWIR. The data collection was performed within 1.5 hours of solar noon in order to limit high zenith angle impacts. An optimization was conducted prior to the start of data collection and any time lighting conditions changed
245 in order to ensure accurate reflectance readings. Data collections were taken 2.5 to 3 feet above the snow surface using a 5 degree field of view optic lens, resulting in a measurement footprint diameter of approximately 6 cm. The collection strategy employed included taking a white reference reading from a pure reflective panel and five readings at different locations on the target surface; the mean of the five readings was used as the reflectance value for that specific location.

250 In this paper, we focus specifically on data collected on 12 February, 2021 as this day had the most stable ambient lighting conditions and resulted in the majority of our snow and reflectance measurements. At the time of the measurements the sky was covered with a high optically thick overcast, and as a result the ambient lighting conditions were generally diffuse. The

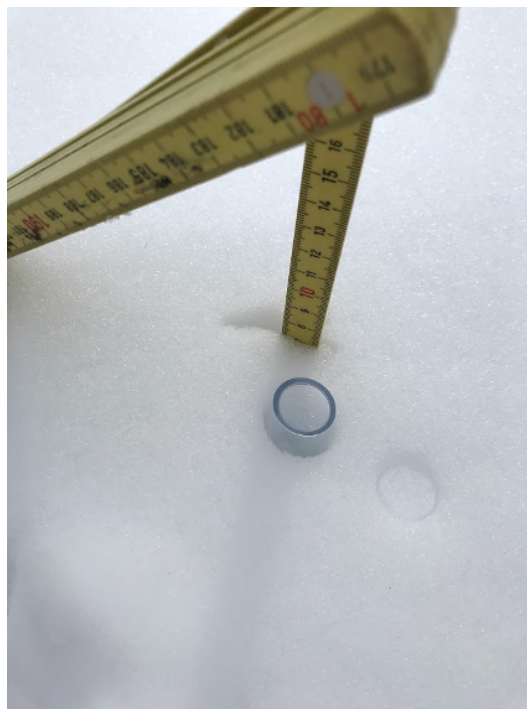


Figure 4. Photograph showing snow sample collection for μ CT analysis.

snow was dry and approximately 34 cm deep, and was roughly characterized as a layer of relatively fresh snow approximately 10 cm deep overlying a layer comprised of larger mixed refrozen snow grain clusters and facets, separated by a 1 cm thick ice crust. To simulate the effects of a shallow snowpack, an aluminum panel painted black was inserted into the snowpack through the snow pit sidewall at three depths (10 cm, 4.75 cm, and 2.5 cm) with care as not to damage the smooth snow surface (e.g., Fig. 5). This panel was strongly absorptive in the visible and NIR spectrum with a constant reflectance of approximately 4 % throughout the entire 350 - 2500 nm spectrum. Since there was no appreciable difference between the measured spectral albedo of the virgin snow (i.e., no inserted panel) and the panel inserted at 10 cm, we limit our analysis to the 4.75 and 2.5 cm panel depths.

2.5 μ CT sampling and Mesh Generation

These snow samples were characterized at the microscale with a cold-hardened Bruker Skyscan 1173 μ CT scanner housed in a -10 °C cold room equipped with a Hamamatsu 130/300 tungsten X-ray source, which produces a fixed conical, polychromatic beam with a spot size of $<5 \mu\text{m}$ and a flat panel sensor camera detector. Each sample was scanned with 38 kV X-rays at 196 mA and a nominal resolution of approximately $20 \mu\text{m}$ as the sample was rotated 180° in 0.6° steps with an exposure time of 300-350 ms. X-rays were detected using a 5 Mp (2240 x 2240) flat panel sensor utilizing 2 x 2 binning, and projection radiographs were averaged over four frames. The resulting 1120 x 1120 pixel radiographs were then reconstructed into 2D



Figure 5. Photograph of the black aluminum panel inserted into the snow pit sidewall approximately 2.5 cm from the surface.

gray-scale horizontal slices using NRecon software (Bruker), which utilizes a modified Feldkamp cone-beam algorithm to produce a vertical stack of gray-scale cross-section images. Image reconstruction processing included sample-specific post alignment, Gaussian smoothing using a kernel size of 2 to reduce noise, sample-specific ring artifact correction of dead pixels, beam hardening correction, and X-ray source thermal drift correction. A cylindrical volume of interest with a diameter of 1.6 cm was selected from the scanned samples in order to eliminate edge effects caused by the sampling process.

Resulting grayscale images are segmented into two phases: air (lowest X-ray absorption), and snow (highest X-ray absorption). Segmenting thresholds for each phase are determined by finding the local minimum between peaks on the histogram showing all grayscale values, and using that value as a global threshold for each scanned sample. The resulting binarized data are despeckled so that any objects less than 2 pixels in diameter were removed.

The final binarized images are then used to construct 3D representations of dry snow samples for input into the RTM. This is accomplished through the use of open-source image processing and 3D visualization software packages accessed through Python (Schroeder et al., 2004; Van der Walt et al., 2014; Sullivan and Kaszynski, 2019). From the binarized images, the

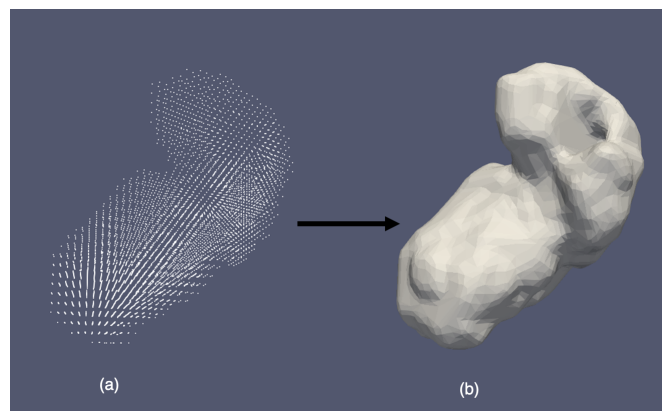


Figure 6. a) Point cloud representation of an example grain. b) surface rendering of the point cloud.

280 first step is to detect and mark individual snow grains. This can prove difficult as the grains are sintered together and their definition can be subjective. However, there is a wide body of literature on grain segmentation methods (e.g., Mangan and Whitaker, 1999; Wang et al., 2012; Theile and Schneebeli, 2011; Hagenmuller et al., 2013, 2014). Here, we use a common grain segmentation threshold technique called watershed segmentation due to its relatively easy implementation, computational efficiency, and accuracy. To apply this method we first combine a stack of binarized images and construct a 3D point cloud sub
285 sample of approximately 800 mm^3 ($\approx 450^3$ voxels) and calculate the Euclidean distance transform of the point cloud. Markers are then generated for the local maxima of the distance to the background. The watershed algorithm treats pixel values as a local topography and floods basins from the markers until basins attributed to different markers meet on watershed lines, which tend to occur along physical grain boundaries. From this, individual grains are extracted from the sample.

To build a full sample mesh, the grains are processed on an individual basis and then combined together to create the
290 full mesh. To process each individual grain, a contour-based surface reconstruction process was developed to generate grain surfaces from the voxels that make up the grain. This method uses a subset of the binary sample array that contains the target grain, including both snow and adjacent air voxels. The subset array is then refined to increase the resolution. A Gaussian filter is applied to smooth the refined array, diminishing pixelated appearance of the voxelized snow-air interface, producing a smooth level set from which to extract the grain surface (Fig. 6). The smoothed level set is then used to define an isosurface at
295 the snow-air boundary, providing control over where the boundary is drawn with respect to the voxels.

Finally, to extract the isosurface from the 3D voxel array, we apply the Marching Cubes method. In this technique, the input volume is divided into a discrete set of cubes. The algorithm then determines how the surface intersects with a given cube, based on the classification of the surrounding vertices and calculates an index for the cube by comparing the sample values at the vertices with the given isosurface value. From these results, it uses a pre-calculated lookup table of various surface-edge
300 intersections possible with the cube. Finally, the algorithm finds the surface-edge intersection through linear interpolation, resulting in a triangulated mesh. The algorithm “marches” through each cube. The original algorithm presented by Lorensen and Cline (1987) can lead to cracks and over the years has been improved by many (Nielson and Hamann, 1991; Scopigno,

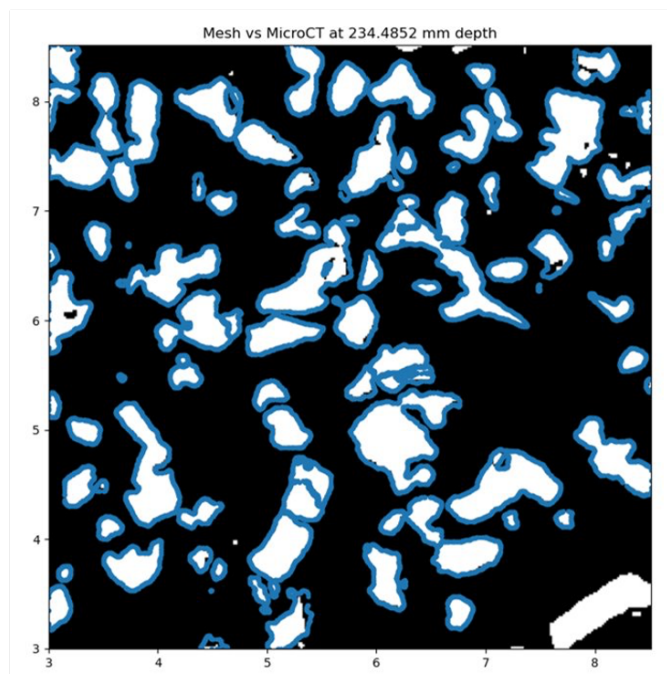


Figure 7. 2D Cross-sectional slice of a binarized μ CT scan with corresponding mesh boundaries superimposed shown as the blue lines.

1994; Natarajan, 1994; Chernyaev, 1995; Lewiner et al., 2003). For this work, we used the adaptation implemented by Lewiner et al. (2003), which improved the algorithm to resolve face and internal ambiguities, extended the lookup table, and guaranteed
305 correct topology. As a final step, each grain is “repaired” to remove any defects and degenerate elements and ensure a manifold surface according to Attene (2010), and then decimated to reduce the overall number of triangles that comprise the surface thereby lowering the computational requirements. Overall, this method appears to accurately characterize the snow within the μ CT sample with computed mesh snow sample densities within 1.5% of snow densities computed from the raw voxels. Figure 7 shows a 2D cross section comparing grain boundaries to the raw pixels of the image and selected example 3D rendered grains
310 are show in Figure 8.

3 Results

3.1 General Evaluation

An initial evaluation of the model is performed by simulating the spectral albedo for two idealized 20 cm deep snowpacks with uniform optical properties throughout. For these snowpacks, the optical properties are determined from 3D meshes generated
315 by two characteristically distinct μ CT samples. One mesh is representative of fresh, fine-grained snow near the surface, and the other of large facets near the bottom of the snowpack (Fig. 9). For each mesh, the total mesh volume is approximately

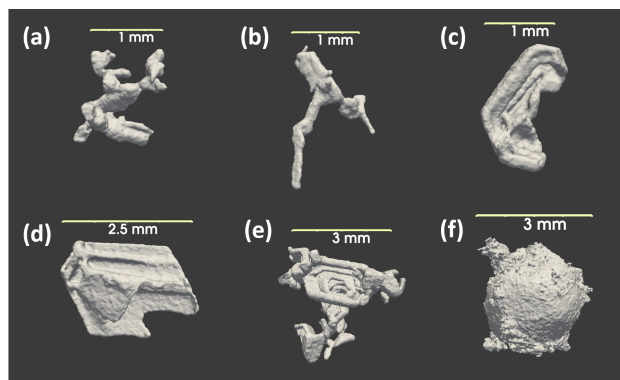


Figure 8. Example 3D renderings of different snow grains. These grains represent a variety of snow types including fresh snow aggregates (a, c), elongated needles (b), and faceted grain fragments (d,e), and sleet (f).

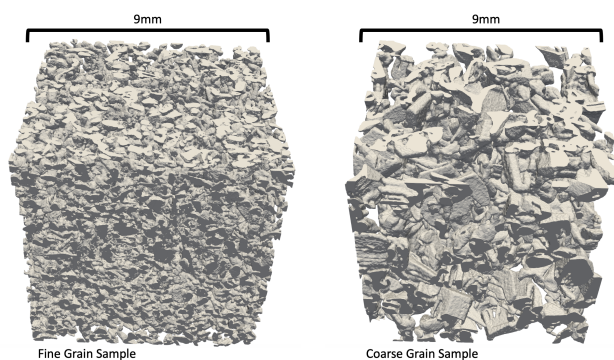


Figure 9. 3D renderings of mesh samples used to generate the optical properties for the general evaluation and snow transmissivity comparisons.

800 mm³. Additional physical and optical properties of the each mesh are presented in Table 1. For each sample, the spectral albedo is computed for wavelengths between 400-1300 nm at 25 nm intervals with diffuse incident radiation. This comparison demonstrates that the model capably reproduces some known behavior of spectral albedo, and specifically, it shows a strong wavelength dependence on snow microstructure that favors the NIR (Fig. 10a). The spectral albedo is relatively uniform between the two snowpacks for the spectral range between 400 and 800 nm, and then the albedos diverge, with a more rapid decrease in albedo for the coarser-grained snow.

We then assess the relationship between simulated spectral albedo and incident zenith angle for the fine grain snow sample at four different wavelengths to evaluate the model's ability to simulate anisotropy in the surface reflectance (Fig. 10b). This analysis shows an exponential increase in albedo at high zenith angles that is most pronounced in the NIR, consistent with observed behavior. This result indicates that the model is capable of simulating surface anisotropy with good fidelity. As a



Table 1. Physical and optical properties of the fine grain and coarse grain mesh samples. Note that SSA and ρ_s are computed directly from the μ CT sample.

Property	Fine Grain	Coarse Grain
SSA ($\text{m}^2 \text{kg}^{-1}$)	19.29	12.85
ρ_s (kg m^{-3})	263	232
γ_{ext} (mm^{-1})	1.86	0.99
F_{ice}	0.44	0.41

related evaluation, the model-simulated DCRF is computed as a function of zenith angle (Fig.11). This analysis reveals that the reflectance is mostly isotropic for zenith angles less than approximately 55° at which point the surface becomes increasingly forward scattering, consistent with previous observational and modeling studies (Kaempfer et al., 2007; Dumont et al., 2010; Xiong et al., 2015; Jiao et al., 2019).

Finally, we use the model to provide an initial assessment of the impacts of snow microstructure on simulated spectral transmissivity. To accomplish this, the optical properties of the μ CT samples in Fig. 9 are used to simulate and compare the spectral transmissivity at varying depths (Fig. 12). The transmissivity is highest at the short, non-absorptive, wavelengths and gradually decreases throughout the NIR, broadly matching quantitative snow transmissivity results reported in Perovich (2007) and Libois et al. (2013). The depth of the 5% transmissivity contour for the fine-grain snow sample is approximately 2.5 cm for the visible, and decreases to approximately 1.5 cm for the NIR (Fig. 12a), indicating that the fine-grain snow optical thickness is on the order of only a few centimeters. In contrast, the transmissivity for the coarse grain snow is increased near the surface, and the depth of the 5 % contour increases to 7.5 cm for the visible and 3 cm for the NIR (Fig. 12b).

3.2 Evaluation against UVD Data

The optical properties used in the 1D RTM were determined from four approximately 800 mm^3 μ CT samples, with each sample representing a 2 cm thick layer within the top 8 cm of the snowpack. The RTM is then configured with 4 layers according to these optical properties (given in Table 2). The top three layers are each 2 cm thick, and the bottom layer is 28 cm thick, such that the entire snow depth amounted to 34 cm. We choose this configuration working under the hypothesis that the snow microstructure below 8 cm had little impact on the measured surface spectral albedo. To simulate the panels, the snowpack depth is modified to be 4.75 and 2.5 cm deep with a 100 % absorptive lower boundary while maintaining the layering corresponding to Table 2.

There is remarkably good agreement between our observations and the model (Fig. 13) and in particular, the model accurately simulates the impact of the inserted panel on the surface albedo for wavelengths shorter than 1000 nm for both the 4.75 and 2.5 cm depths. The model and observations diverge after 1200 nm, in particular, the simulated albedo is substantially higher in this range than measured. We hypothesize that this is primarily due to the phase function approximation computed from the rendered snow grains. Additional simulations that use the phase function computed from idealized spheres and columns support this

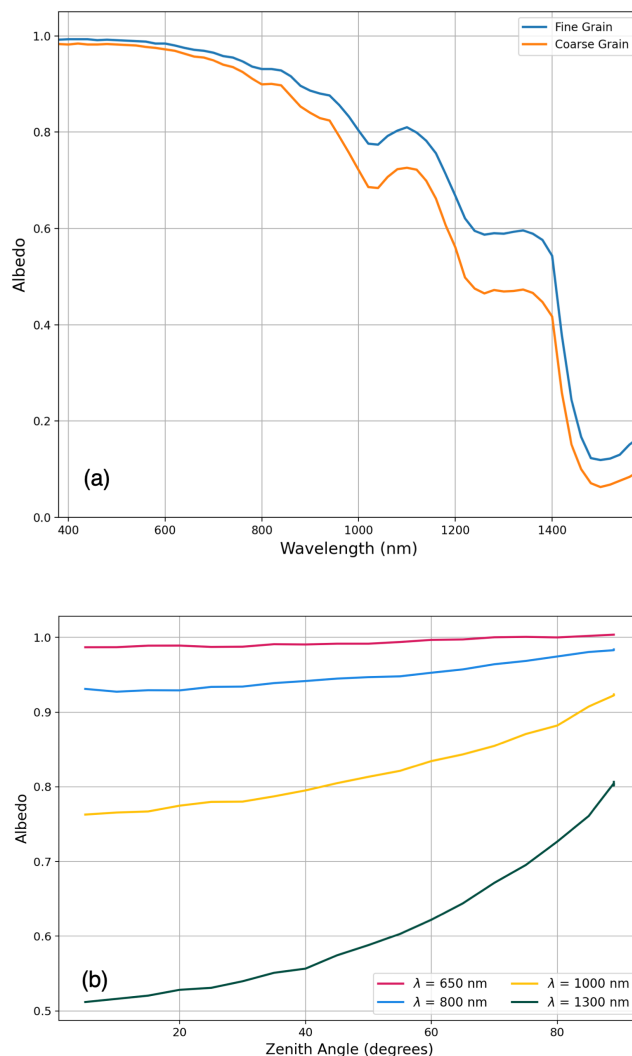


Figure 10. a) Simulated spectral albedo for fine grain and coarse grain snow samples for 100% diffuse radiation. b) Simulated spectral albedo as a function of incident zenith angle for selected wavelengths. Note that both simulations were run with 25000 photons.

hypothesis by showing that the spectral albedo is sensitive to the phase function at these wavelengths (not shown). This suggests that future improvements in the grain segmentation and surface rendering algorithms could improve these results in the NIR. Alternatively, this difference possibly illustrates the limits of the geometric optics approximation as the approximate particle

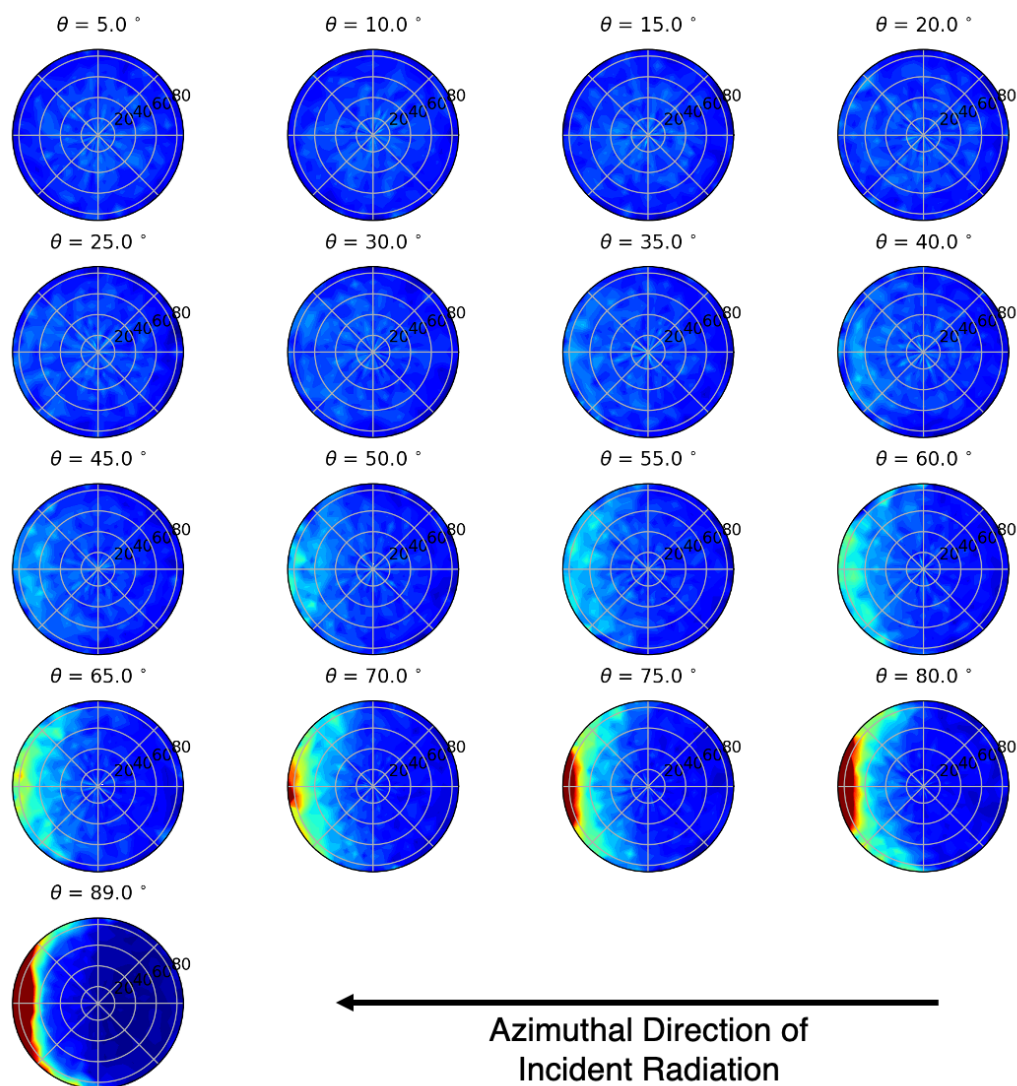


Figure 11. Polar plots of DCRF at 1000 nm for incident zenith angles ranging from 5 - 89°. Reflected azimuthal direction is on the theta axis, and reflected zenith angle if on the r axis. Color scale ranges from 0-1.5.

355 size parameter is < 1000 for $\lambda > 1000$ nm. Overall, this initial evaluation against the ASD data is promising and suggests that this framework can be used to better understand the impacts of snow microstructure on reflectance and transmissivity.

3.3 Snow optical and physical properties

A final analysis is performed to determine how strongly common snow physical properties relate to the simulated optical properties from this framework. Specifically, we compare snow specific surface area (SSA) and snow sample density (ρ_s) to

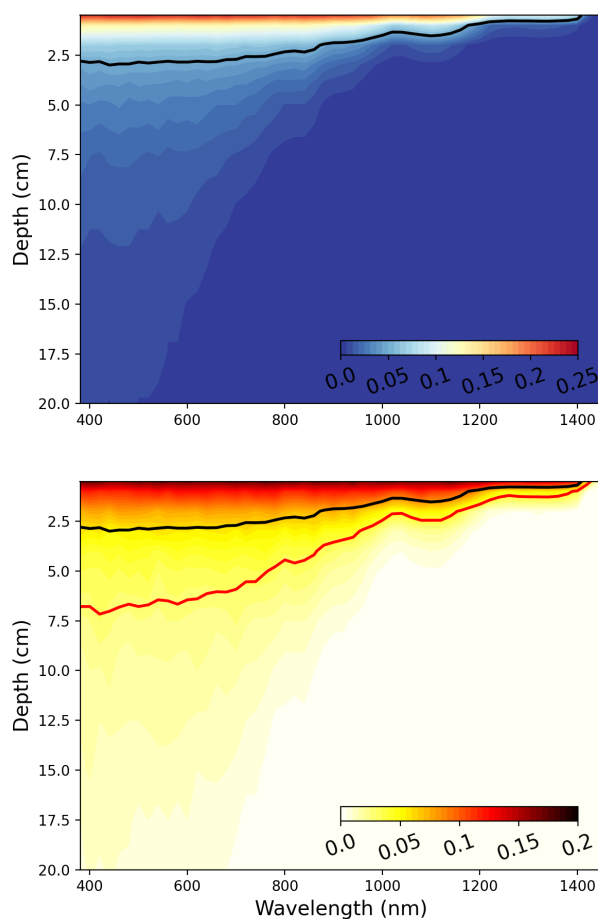


Figure 12. a) Simulated transmissivity of the fine grain snow sample contoured as a function of depth and wavelength. b) Transmissivity difference between the coarse grain and fine grain samples as a function of wavelength and depth. The 5% transmissivity contour is plotted for the fine grain (black) and coarse grain (red) samples.

Table 2. Physical and simulated optical properties of the top 8 cm of snow measured at the UVD site on February 12 2021. SSA and ρ_s are computed directly from the μ CT sample. Note that the depths correspond to the RTM model depths for the virgin snow calculation.

depth [cm]	SSA ($\text{m}^2 \text{kg}^{-1}$)	ρ_s (kg m^{-3})	γ_{ext} (mm^{-1})	F_{ice}
1 (32-34)	26.1	147	1.39	0.35
2 (30-32)	27.2	178	1.77	0.38
3 (28-30)	21.12	250	2.04	0.47
4 (0-28)	18.44	287	1.86	0.51

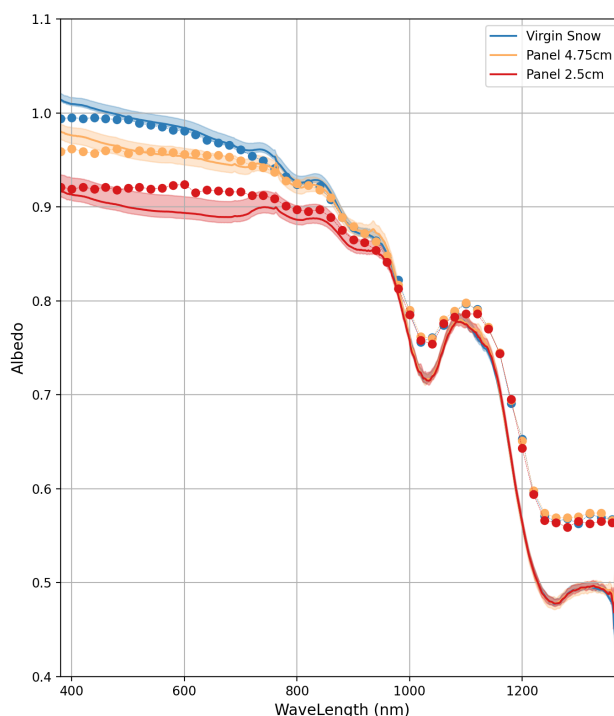


Figure 13. Simulated and observed spectral albedo at UVD for three different snow depths. Solid lines indicate observations and dotted lines indicate simulations. The shading around the observations indicates the inter-quartile range of the measurements computed from the five snow and two reference scans collected during each measurement, providing an assessment of measurement uncertainty. Mean RMSE of simulated albedo over 400-1600nm is equal to 0.06.

360 γ_{ext} and F_{ice} . This analysis is performed using several μ CT sample volumes collected on different dates, at different locations, and for various snow types. Note that each μ CT sample is approximately 800 mm³ and the sample SSA and ρ_s are determined from the μ CT 3D rendering. This analysis reveals that F_{ice} has a very robust relationship with snow density (Fig. 14a) described by the linear fit:

$$F_{ice} = 0.00074\rho_s + 0.25, \quad (21)$$

365 with $r^2 = 0.81$. In contrast, while γ_{ext} generally seems to increase as a function of SSA, this relationship is not as well constrained as the relationship between ρ_s and F_{ice} (Fig. 14b). Instead, we find that γ_{ext} is generally better approximated by a multivariate regression function that includes both SSA and density:

$$\gamma_{ext} = 0.077SSA + 0.0028\rho_s - 0.59, \quad (22)$$



with $r^2 = 0.26$. Interestingly, this relationship can be improved substantially by removing the ice-crust samples from the
370 dataset. This change modifies eq. 22 to:

$$\gamma_{ext} = 0.085SSA + 0.0062\rho_s - 1.51, \quad (23)$$

and increases r^2 to from 0.25 to 0.79. This relationship dictates that the extinction coefficient increases both as a function of
SSA and ρ_s , indicating that the highest extinction coefficients will be associated with small, tightly packed snow grains. This
is qualitatively consistent, though not directly comparable, with analytical formulations in Kokhanovsky and Zege (2004), who
375 show the extinction coefficient is related to both surface area and grain concentration, which is a good proxy for snow density.
In contrast, with ice-crusts the extinction coefficient is more strongly related to SSA, and largely independent of ρ_s , leading to
low extinction coefficients despite very high snow densities, counteracting the relationships described in equations 22,23. This
behavior can be attributed to the fact that for crust layers, snow density is no longer a good proxy for particle concentration
and therefore does not significantly affect the extinction coefficient. Overall, these results suggest that commonly observed
380 physical snow properties can be used to approximate optical properties in conjunction with an appropriate phase function for
the medium photon-tracking RTM model for non-crust snow layers.

To further assess how these two specific snow optical properties, γ_{ext} and F_{ice} , affect the greater simulated spectral trans-
missivity, we perform a sensitivity analysis by comparing the 5% transmissivity contour depth for three fractional ice paths:
0.30, 0.46, 0.69 at two fixed γ_{ext} values: 2.34, 0.81 mm^{-1} . The two γ_{ext} values correspond to the max, min values found in the
385 previous analysis and presented in Fig. 14b. The three F_{ice} values correspond to the max, min, and mean values (Fig. 14a). We
compare the influence of F_{ice} at both the max and min γ_{ext} values, since we anticipate the strength of its influence will vary
according to γ_{ext} . While we pair the maximum γ_{ext} with the F_{ice} , we note that high values of γ_{ext} are more likely to coincide
with high values of F_{ice} due to the shared dependence of these variables on snow density in most snowpacks.

The results of this analysis indicate that γ_{ext} has a much larger impact on snow transmissivity than F_{ice} . This is unsurprising
390 due to the highly scattering nature of snow. In particular the snow medium is much more transmissive at the minimum γ_{ext}
value with the 5 % transmissivity contours exceeding 7 cm in the visible and 3 cm in the NIR. This is in contrast to the
transmissivity of the maximum extinction coefficient, which never exceeds 4 cm of depth (Fig. 15). F_{ice} can either amplify
or dampen the effect of γ_{ext} in the NIR, with lower values of F_{ice} leading to an increase in transmissivity at a given depth
compared to high values of F_{ice} .

395 4 Discussion

One key objective of this work is to expand beyond determining snow optical properties from a specified distribution of grains
with idealized shapes, and instead represent snow as an organized structure in determining them. One snow type where this
approach may be particularly advantageous is in understanding the optical properties of snow crust layers, which do not fit
easily into the collection of particles or air bubbles approximation. This is supported by our finding that γ_{ext} is very well

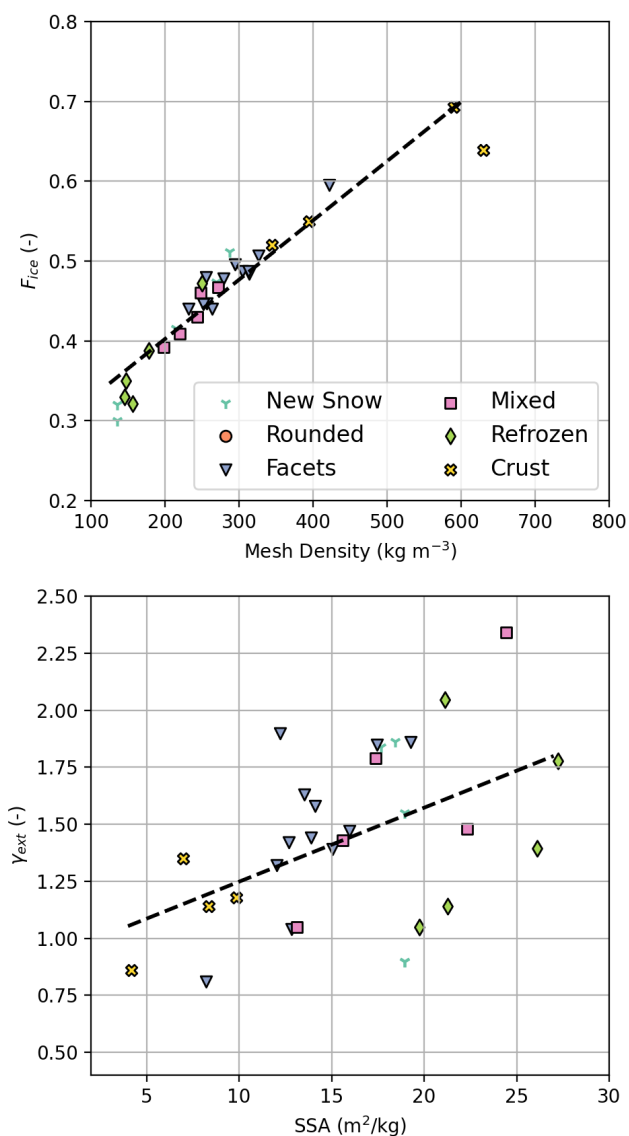


Figure 14. Optical properties for $\lambda=900\text{nm}$ computed from μCT photon-tracking compared against sample physical properties. a) F_{ice} vs. ρ_s and b) γ_{ext} vs. SSA. Linear regression lines are shown in black dashed lines. Note that the regression line plotted on (b) is a single-parameter regression line for illustrative purposes, and not the multi-parameter regression discussed in the text. Snow grain forms were determined through visual assessment during snow pit analysis.

400 approximated with a multivariate regression of SSA and ρ_s for all observed snow types except for crusts, which exhibited the

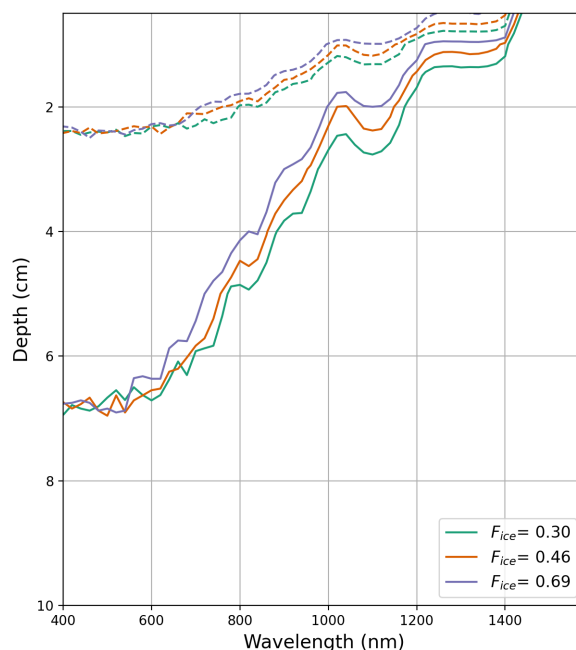


Figure 15. Depth of simulated 5% transmissivity contour as a function of wavelength for varying F_{ice} at two extinction coefficient: $\gamma_{ext} = 0.81$ (Solid lines) and $\gamma_{ext} = 2.34$ (Dashed lines).

highest snow densities and the lowest extinction coefficients and SSAs. Another snow type this approach may be well suited for is highly aged snow that has metamorphosed into a collection of large irregularly shaped grain clusters and pore spaces.

While ideally, the optical properties would vary slightly with wavelength due to the impact of absorption on γ_{ext} and the phase function, we chose to leave the optical properties independent of wavelength. This choice is made entirely to reduce the computational burden of running the photon-tracking model for several wavelengths. Cursory sensitivity tests performed to assess the impact of this choice on the optical properties supported the use of wavelength-independent optical properties, as both $p(\cos\Theta)$ and γ_{ext} exhibited generally a negligible dependence on wavelength for $\lambda > 1400$. We suspect that this is due to the fact that a ray is much more likely to be scattered at an air/ice boundary than by absorption within the particle (i.e., snow has a high single scattering albedo). This may not be the case for all snow types, in particular for the NIR wavelengths within very large grains, and is worthy of future exploration.



5 Conclusions

In this work we have presented a blended photon-tracking radiative transfer model in an effort to better understand the complicated influence of snowpack microstructure on snow spectral transmissivity in the geometric optics limit. A foundational goal of this modeling approach is to expand upon previous approaches aimed at incorporating 3D renderings of real snow
415 microstructure into radiative transfer models for snowpacks of arbitrary depth, while maintaining the Monte Carlo aspects of the model. To accomplish this, existing methods for simulated photon interactions with rendered elements are employed to determine key optical properties of the snow (Grundy et al., 2000; Kaempfer et al., 2007; Xiong et al., 2015).

An evaluation of this framework for consistency with known behavior of spectral snow albedo revealed that this framework can successfully reproduce the dependency of spectral albedo and grain size, as well as the surface anisotropy at high incident
420 zenith angles. Furthermore, a comparison of the simulated snow albedo against spectroradiometer measurements collected in the field over snow with varying depths indicate that the model can simulate the effects of an underlying surface on spectral albedo with high accuracy.

In comparing two different snow samples, it was revealed that snow microstructure has a large impact on snow transmissivity in the visible spectrum and near the snow surface, increasing the 5 % transmissivity depth from approximately 4 cm for a fine
425 grain snow sample to 7.5 cm depth for a coarse grain sample. A brief sensitivity analysis of the optical properties revealed that lowering the medium extinction coefficient acted to reduce the albedo and increase transmissivity in the visible bands, while the fractional ice path (F_{ice}) impacted the rate at which albedo and transmissivity decreased as a function of wavelength in the NIR. Accordingly, we anticipate that snowpacks made up of large grains with low fractional ice-paths will be the most transmissive.

Overall, while current efforts are focused on using this model to better understand snow transmissivity, it shows promise as
430 a broadly applicable snow RTM that has a strong direct connection to μ CT snow samples. While currently, it is limited to the geometric optics approximation for clean snow and unpolarized radiation, ongoing and anticipated future efforts are aimed at improving the grain segmentation and rendering process, incorporating polarization, parameterizing diffraction, and including light absorbing particulates (LAPs). In particular, recent multiphase image segmentation techniques (e.g., West et al., 2018)
435 could be used to better separate snow, air, and LAPs in a μ CT sample allowing for the impact of LAPs to be determined through ray-tracing. Furthermore, because the model operates entirely as a photon-tracking model, it is a natural fit with macro-scale ray-tracing and therefore could be used to investigate the reflectance of rough snow surfaces such as sun cups or sastrugi.

Code and data availability. The mesh generation and RTM code with associated documentation is available in preliminary 'as is' format on Github at (<https://github.com/wxted/CRREL-GOSRT.git>). Sample data files used to generate figure 9a is available on Github as sample
440 data. Additional limited sample data, including rendered microCT meshes, and spectroradiometer data used for this paper are available upon request



445 *Author contributions.* Theodore Letcher performed a majority of the model physics, structural development, and coding, in addition to coordinating the model analysis and manuscript preparation. Julie Parno led research and coding efforts related to the 3D mesh generation and rendering and assisted in general coding, she also coordinated a majority of the fieldwork activity. Zoe Courville provided research support, participated in snow sampling and coordinated μ CT analysis. Lauren Farnsworth performed a large portion of μ CT scans and a majority of the μ CT image post processing and analysis. Jason Olivier participated in fieldwork and provided background on the ASD instrumentation and sampling for the manuscript. Theodore, Julie, and Jason performed the RTM simulations and assisted in code debugging. All authors provided writing support for the manuscript.

Competing interests. The authors declare that no competing interests are present

450 *Acknowledgements.* We wish to acknowledge Dr. Arnold Song from Dartmouth College in Hanover New Hampshire for providing relevant code examples to facilitate 3D shape rendering. We also wish to thank Taylor Hodgdon from CRREL for providing occasional support and advice on using Python to perform snow grain segmentation and rendering. Finally, we wish to thank Dr. Bert Davis, and Dr. Ned Bair for providing valuable initial feedback on the manuscript. Funding support for this research was provided by the U.S. Army Engineer Research and Development Center (ERDC) Cold Weather Military Research project. **Place Holder to thank reviewers**



455 References

- Adolph, A. C., Albert, M. R., Lazarcik, J., Dibb, J. E., Amante, J. M., and Price, A.: Dominance of grain size impacts on seasonal snow albedo at open sites in New Hampshire, *Journal of Geophysical Research: Atmospheres*, 122, 121–139, 2017.
- Aoki, T., Aoki, T., Fukabori, M., Hachikubo, A., Tachibana, Y., and Nishio, F.: Effects of snow physical parameters on spectral albedo and bidirectional reflectance of snow surface, *Journal of Geophysical Research: Atmospheres*, 105, 10 219–10 236, 2000.
- 460 Attene, M.: A lightweight approach to repairing digitized polygon meshes, *The visual computer*, 26, 1393–1406, 2010.
- Bair, E. H., Rittger, K., Skiles, S. M., and Dozier, J.: An examination of snow albedo estimates from MODIS and their impact on snow water equivalent reconstruction, *Water Resources Research*, 55, 7826–7842, 2019.
- Bohren, C. F. and Beschta, R. L.: Snowpack albedo and snow density, *Cold Regions Science and Technology*, 1, 47–50, 1979.
- Chernyaev, E.: Marching cubes 33: Construction of topologically correct isosurfaces, Tech. rep., 1995.
- 465 Dang, C., Fu, Q., and Warren, S. G.: Effect of snow grain shape on snow albedo, *Journal of the Atmospheric Sciences*, 73, 3573–3583, 2016.
- Dang, C., Zender, C. S., and Flanner, M. G.: Intercomparison and improvement of two-stream shortwave radiative transfer schemes in Earth system models for a unified treatment of cryospheric surfaces, *The Cryosphere*, 13, 2325–2343, 2019.
- Déry, S. J. and Brown, R. D.: Recent Northern Hemisphere snow cover extent trends and implications for the snow-albedo feedback, *Geophysical Research Letters*, 34, 2007.
- 470 Dickinson, R. E.: Biosphere atmosphere transfer scheme (BATS) version 1e as coupled to the NCAR community climate model, NCAR Tech. Note TH-387+ STR, 1993.
- Doherty, S., Warren, S., Grenfell, T., Clarke, A., and Brandt, R.: Light-absorbing impurities in Arctic snow, *Atmospheric Chemistry and Physics*, 10, 11 647–11 680, 2010.
- Dumont, M., Brissaud, O., Picard, G., Schmitt, B., Gallet, J.-C., and Arnaud, Y.: High-accuracy measurements of snow Bidirectional Re-
- 475 flectance Distribution Function at visible and NIR wavelengths—comparison with modelling results, *Atmospheric Chemistry and Physics*, 10, 2507–2520, 2010.
- Dumont, M., Brun, E., Picard, G., Michou, M., Libois, Q., Petit, J., Geyer, M., Morin, S., and Josse, B.: Contribution of light-absorbing impurities in snow to Greenland’s darkening since 2009, *Nature Geoscience*, 7, 509–512, 2014.
- Dumont, M., Flin, F., Malinka, A., Brissaud, O., Hagenmuller, P., Lapalus, P., Lesaffre, B., Dufour, A., Calonne, N., Rolland du Roscoat,
- 480 S., et al.: Experimental and model-based investigation of the links between snow bidirectional reflectance and snow microstructure, *The Cryosphere*, 15, 3921–3948, 2021.
- Flanner, M. G. and Zender, C. S.: Linking snowpack microphysics and albedo evolution, *Journal of Geophysical Research: Atmospheres*, 111, 2006.
- Flanner, M. G., Shell, K. M., Barlage, M., Perovich, D. K., and Tschudi, M.: Radiative forcing and albedo feedback from the Northern
- 485 Hemisphere cryosphere between 1979 and 2008, *Nature Geoscience*, 4, 151–155, 2011.
- Gardner, A. S. and Sharp, M. J.: A review of snow and ice albedo and the development of a new physically based broadband albedo parameterization, *Journal of Geophysical Research: Earth Surface*, 115, 2010.
- Grenfell, T. C. and Perovich, D. K.: Radiation absorption coefficients of polycrystalline ice from 400–1400 nm, *Journal of Geophysical Research: Oceans*, 86, 7447–7450, 1981.
- 490 Grundy, W., Douté, S., and Schmitt, B.: A Monte Carlo ray-tracing model for scattering and polarization by large particles with complex shapes, *Journal of Geophysical Research: Planets*, 105, 29 291–29 314, 2000.



- Hagenmuller, P., Chambon, G., Lesaffre, B., Flin, F., and Naaim, M.: Energy-based binary segmentation of snow microtomographic images, *Journal of Glaciology*, 59, 859–873, 2013.
- Hagenmuller, P., Chambon, G., Flin, F., Morin, S., and Naaim, M.: Snow as a granular material: assessment of a new grain segmentation
495 algorithm, *Granular Matter*, 16, 421–432, 2014.
- Hall, A.: The role of surface albedo feedback in climate, *Journal of Climate*, 17, 1550–1568, 2004.
- Haussener, S., Gergely, M., Schneebeli, M., and Steinfeld, A.: Determination of the macroscopic optical properties of snow based on exact morphology and direct pore-level heat transfer modeling, *Journal of Geophysical Research: Earth Surface*, 117, 2012.
- He, C. and Flanner, M.: Snow Albedo and Radiative Transfer: Theory, Modeling, and Parameterization, in: *Springer Series in Light Scatter-*
500 *ing*, pp. 67–133, Springer, 2020.
- Iaquinta, J., Isaka, H., and Personne, P.: Scattering phase function of bullet rosette ice crystals, *Journal of Atmospheric Sciences*, 52, 1401–1413, 1995.
- Ishimoto, H., Adachi, S., Yamaguchi, S., Tanikawa, T., Aoki, T., and Masuda, K.: Snow particles extracted from X-ray computed micro-
tomography imagery and their single-scattering properties, *Journal of Quantitative Spectroscopy and Radiative Transfer*, 209, 113–128,
505 2018.
- Iwabuchi, H.: Efficient Monte Carlo methods for radiative transfer modeling, *Journal of the atmospheric sciences*, 63, 2324–2339, 2006.
- Jacques, S. L.: Monte Carlo modeling of light transport in tissue (steady state and time of flight), in: *Optical-thermal response of laser-*
irradiated tissue, pp. 109–144, Springer, 2010.
- Jiao, Z., Ding, A., Kokhanovsky, A., Schaaf, C., Bréon, F.-M., Dong, Y., Wang, Z., Liu, Y., Zhang, X., Yin, S., et al.: Development of a
510 snow kernel to better model the anisotropic reflectance of pure snow in a kernel-driven BRDF model framework, *Remote Sensing of Environment*, 221, 198–209, 2019.
- Kaempfer, T. U., Hopkins, M., and Perovich, D.: A three-dimensional microstructure-based photon-tracking model of radiative transfer in snow, *Journal of Geophysical Research: Atmospheres*, 112, 2007.
- Kokhanovsky, A. A. and Zege, E. P.: Scattering optics of snow, *Applied Optics*, 43, 1589–1602, 2004.
- 515 Letcher, T. W. and Minder, J. R.: Characterization of the simulated regional snow albedo feedback using a regional climate model over complex terrain, *Journal of Climate*, 28, 7576–7595, 2015.
- Lewiner, T., Lopes, H., Vieira, A. W., and Tavares, G.: Efficient implementation of marching cubes’ cases with topological guarantees, *Journal of graphics tools*, 8, 1–15, 2003.
- Libois, Q., Picard, G., France, J., Arnaud, L., Dumont, M., Carmagnola, C., and King, M.: Influence of grain shape on light penetration in
520 snow, *The Cryosphere*, 7, 1803–1818, 2013.
- Lorensen, W. E. and Cline, H. E.: Marching cubes: A high resolution 3D surface construction algorithm, *ACM siggraph computer graphics*, 21, 163–169, 1987.
- Macke, A., Mueller, J., and Raschke, E.: Single scattering properties of atmospheric ice crystals, *Journal of Atmospheric Sciences*, 53, 2813–2825, 1996.
- 525 Malinka, A. V.: Light scattering in porous materials: Geometrical optics and stereological approach, *Journal of Quantitative Spectroscopy and Radiative Transfer*, 141, 14–23, 2014.
- Mangan, A. P. and Whitaker, R. T.: Partitioning 3D surface meshes using watershed segmentation, *IEEE Transactions on Visualization and Computer Graphics*, 5, 308–321, 1999.
- Natarajan, B. K.: On generating topologically consistent isosurfaces from uniform samples, *The Visual Computer*, 11, 52–62, 1994.



- 530 Nielson, G. M. and Hamann, B.: The asymptotic decider: resolving the ambiguity in Marching Cubes., in: IEEE visualization, vol. 91, pp. 83–91, 1991.
- Painter, T. H., Bryant, A. C., and Skiles, S. M.: Radiative forcing by light absorbing impurities in snow from MODIS surface reflectance data, *Geophysical Research Letters*, 39, 2012.
- Perovich, D. K.: Light reflection and transmission by a temperate snow cover, *Journal of Glaciology*, 53, 201–210, 2007.
- 535 Perovich, D. K. and Govoni, J. W.: Absorption coefficients of ice from 250 to 400 nm, *Geophysical Research Letters*, 18, 1233–1235, 1991.
- Saito, M., Yang, P., Loeb, N. G., and Kato, S.: A novel parameterization of snow albedo based on a two-layer snow model with a mixture of grain habits, *Journal of the Atmospheric Sciences*, 76, 1419–1436, 2019.
- Schroeder, W. J., Lorensen, B., and Martin, K.: The visualization toolkit: an object-oriented approach to 3D graphics, Kitware, 2004.
- Scopigno, R.: A modified look-up table for implicit disambiguation of Marching Cubes, *The visual computer*, 10, 353–355, 1994.
- 540 Shi, T., Cui, J., Chen, Y., Zhou, Y., Pu, W., Xu, X., Chen, Q., Zhang, X., and Wang, X.: Enhanced light absorption and reduced snow albedo due to internally mixed mineral dust in grains of snow, *Atmospheric Chemistry and Physics*, 21, 6035–6051, 2021.
- Skiles, S. M. and Painter, T. H.: Toward understanding direct absorption and grain size feedbacks by dust radiative forcing in snow with coupled snow physical and radiative transfer modeling, *Water Resources Research*, 55, 7362–7378, 2019.
- Skiles, S. M., Painter, T. H., Deems, J. S., Bryant, A. C., and Landry, C. C.: Dust radiative forcing in snow of the Upper Colorado River
- 545 Basin: 2. Interannual variability in radiative forcing and snowmelt rates, *Water Resources Research*, 48, 2012.
- Skiles, S. M., Painter, T. H., Belnap, J., Holland, L., Reynolds, R. L., Goldstein, H. L., and Lin, J.: Regional variability in dust-on-snow processes and impacts in the Upper Colorado River Basin, *Hydrological Processes*, 29, 5397–5413, 2015.
- Stamnes, K. and Stamnes, J. J.: Radiative transfer in coupled environmental systems: an introduction to forward and inverse modeling, John Wiley & Sons, 2016.
- 550 Sullivan, C. B. and Kaszynski, A.: PyVista: 3D plotting and mesh analysis through a streamlined interface for the Visualization Toolkit (VTK), *Journal of Open Source Software*, 4, 1450, <https://doi.org/10.21105/joss.01450>, 2019.
- Thackeray, C. W. and Fletcher, C. G.: Snow albedo feedback: Current knowledge, importance, outstanding issues and future directions, *Progress in Physical Geography*, 40, 392–408, 2016.
- Theile, T. and Schneebeli, M.: Algorithm to decompose three-dimensional complex structures at the necks: tested on snow structures, *IET*
- 555 *Image Processing*, 5, 132–140, 2011.
- Van der Walt, S., Schönberger, J. L., Nunez-Iglesias, J., Boulogne, F., Warner, J. D., Yager, N., Gouillart, E., and Yu, T.: scikit-image: image processing in Python, *PeerJ*, 2, e453, 2014.
- Verseghy, D. L.: CLASS—A Canadian land surface scheme for GCMs. I. Soil model, *International Journal of Climatology*, 11, 111–133, 1991.
- 560 Vionnet, V., Brun, E., Morin, S., Boone, A., Faroux, S., Moigne, P. L., Martin, E., and Willemet, J.-M.: The detailed snowpack scheme Crocus and its implementation in SURFEX v7. 2, *Geoscientific Model Development*, 5, 773–791, 2012.
- Wang, X., Gillibert, L., Flin, F., and Coeurjolly, D.: Curvature-driven volumetric segmentation of binary shapes: an application to snow microstructure analysis, in: Proceedings of the 21st International Conference on Pattern Recognition (ICPR2012), pp. 742–745, IEEE, 2012.
- 565 Warren, S. G.: Can black carbon in snow be detected by remote sensing?, *Journal of Geophysical Research: Atmospheres*, 118, 779–786, 2013.



- Warren, S. G. and Brandt, R. E.: Optical constants of ice from the ultraviolet to the microwave: A revised compilation, *Journal of Geophysical Research: Atmospheres*, 113, 2008.
- Warren, S. G. and Wiscombe, W. J.: A model for the spectral albedo of snow. II: Snow containing atmospheric aerosols, *Journal of Atmospheric Sciences*, 37, 2734–2745, 1980.
- 570 West, B. A., Hodgdon, T. S., Parno, M. D., and Song, A. J.: Improved workflow for unguided multiphase image segmentation, *Computers & geosciences*, 118, 91–99, 2018.
- Whitney, B. A.: Monte Carlo radiative transfer, in: *Fluid Flows To Black Holes: A Tribute to S Chandrasekhar on His Birth Centenary*, pp. 151–176, World Scientific, 2011.
- 575 Wiscombe, W. J.: Improved Mie scattering algorithms, *Applied optics*, 19, 1505–1509, 1980.
- Wiscombe, W. J. and Warren, S. G.: A model for the spectral albedo of snow. I: Pure snow, *Journal of Atmospheric Sciences*, 37, 2712–2733, 1980.
- Xiong, C., Shi, J., Ji, D., Wang, T., Xu, Y., and Zhao, T.: A new hybrid snow light scattering model based on geometric optics theory and vector radiative transfer theory, *IEEE Transactions on Geoscience and Remote Sensing*, 53, 4862–4875, 2015.
- 580 Yang, P. and Liou, K.: Geometric-optics–integral-equation method for light scattering by nonspherical ice crystals, *Applied Optics*, 35, 6568–6584, 1996.